*American Mineralogist, Volume 108, pages 1149–1160, 2023*

# UV/Vis single-crystal spectroscopic investigation of almandine-pyrope and almandine-spessartine solid solutions: Part I. Spin-forbidden $Fe^{2+,3+}$ and $Mn^{2+}$ electronic-transition energies, crystal chemistry, and bonding behavior

**Charles A. Geiger[1,*], Michail N. Taran[2], and George R. Rossman[3]**

[1]Department of Chemistry and Physics of Materials, University of Salzburg, Jakob Haringer Str. 2a, A-5020 Salzburg, Austria
[2]M.P. Semenenko Institute of Geochemistry and Mineralogy and Ore Formation, National Academy of Sciences of Ukraine, Palladin Avenue 34, 03142 Kyiv-142, Ukraine
[3]Division of Geological and Planetary Sciences, California Institute of Technology, Pasadena, California 91125-2500, U.S.A.

## Abstract

Aluminosilicate garnet is an excellent phase to research solid-solution behavior in silicates. Natural almandine-pyrope, $\{Fe^{2+}_{3x},Mg_{3-3x}\}[Al_2](Si_3)O_{12}$, and almandine-spessartine, $\{Fe^{2+}_{3x},Mn^{2+}_{3-3x}\}[Al_2](Si_3)O_{12}$, crystals were measured by UV/Vis/NIR (~29 000 to 10 000 $cm^{-1}$) optical absorption spectroscopy using a microscope. The spectra and changes in energy of several $Fe^{2+}$ and $Mn^{2+}$ spin-forbidden electronic transitions of different wavenumber were analyzed as a function of garnet composition across both binaries. The spectra of Alm-Pyp garnets are complex and show several $Fe^{2+}$ and $Fe^{3+}$ transitions manifested as overlapping absorption bands whose intensities depend on composition. There are differences in energy behavior for the various electronic transitions, whereby lower wavenumber $Fe^{2+}$ transitions decrease slightly in energy with increasing pyrope component and those of higher wavenumber increase. The spectra of Alm-Sps solid solutions show both $Fe^{2+}$ and $Mn^{2+}$ spin-forbidden bands depending upon the garnet composition. The variations in energy of the different wavenumber $Fe^{2+}$ transitions are unlike those observed in Alm-Pyp garnets. The three lowest wavenumber electronic transitions appear to vary the most in energy across the Alm-Sps join compared to those at higher wavenumber. Four narrow and relatively intense $Mn^{2+}$ spin-forbidden bands between 23 000 and 25 000 $cm^{-1}$ can be observed in many Sps-Alm garnets. Their transition energies may increase or decrease across the join, but scatter in the data prohibits an unequivocal determination. A consistent crystal-chemical model and $Fe^{2+}$-O bond behavior, based on published diffraction and spectroscopic results, can be constructed for the Alm-Pyp binary but not for the Alm-Sps system. The spectra of the former garnets often show the presence of high-wavenumber spin-forbidden bands that can be assigned to electronic transitions of $Fe^{3+}$ occurring at the octahedral site. The most prominent band lies between 27 100 and 27 500 $cm^{-1}$ depending on the garnet composition. $Fe^{3+}$-$O^{2-}$ bonding is analyzed using Racah parameters. State-of-the-art electronic structure calculations are needed to understand the precise physical nature of the electronic transitions in garnet and to interpret better UV/Vis/NIR spectra.

**Keywords:** UV/Vis/NIR spectroscopy, garnet, solid solutions, electronic spin-forbidden transitions, crystal chemistry

## Introduction

Aluminosilicate garnet, general formula $\{X_3\}[Al_2](Si_3)O_{12}$, where X = Mg, $Fe^{2+}$, $Mn^{2+}$, and Ca, is a key rock-forming mineral occurring in different geologic settings. Many upper-mantle and some crustal garnets are largely pyrope-almandine solid solutions, $\{Mg_{3x}Fe^{2+}_{3-3x}\}[Al_2](Si_3)O_{12}$, and spessartine-almandine garnets, $\{Mn^{2+}_{3x}Fe^{2+}_{3-3x}\}[Al_2](Si_3)O_{12}$, occur in certain crustal granites and pegmatites. Atomic mixing at {X} can be complete for both binaries as shown by compositional analyses of natural garnets (Boeke 1914; Sobolev 1964) and the successful laboratory synthesis of crystals along both joins at elevated pressures and temperatures (e.g., Geiger and Feenstra 1997).

Investigation of the solid-solution behavior of aluminosilicate garnets, both at the micro- and macroscopic scale, is a long, continuing work in progress (Geiger 2008, 2016) and much still needs to be researched. A fundamental problem is in trying to understand the nature of local structural heterogeneity that arises through the exchange of different atoms of varying sizes and electronic properties. Local $X^{2+}$-O chemical bonds must vary slightly as a function of crystal composition. Garnet is an excellent phase to study solid solutions, because $Fe^{2+}$, Mg, and $Mn^{2+}$ mix at the single crystallographic {X} site. All three cations have relatively similar ionic radii, but Mg does not have *d* electrons unlike $Fe^{2+}$ ($3d^6$) and $Mn^{2+}$ ($3d^5$). The chemical-bonding behavior of the latter two transition metals with oxygen should differ between each other and both most certainly with respect to the alkaline Mg cation. A notable crystal-chemical feature of the aluminosilicate garnets is the anisotropic vibrational behavior of the different $X^{2+}$ cations and their probable anharmonic potentials (Geiger 2013). To understand a wide range of atomic-scale and bonding behavior in crystals various spectroscopic measurements are necessary (Geiger 2004).

Optical absorption spectroscopy is a powerful tool for in-

* E-mail: charles.geiger@univie.ac.at. Orcid 0000-0001-9212-354X

0003-004X/23/0006–1149$05.00/DOI: https://doi.org/10.2138/am-2022-8499

vestigating the electronic states of atoms and chemical-bonding behavior. There have been several studies made on different aluminosilicate garnets relating to the electronic absorption bands arising from different transition metals in their various oxidation states, as recorded in the UV/Vis/NIR spectral regions (e.g., Clark 1957; Manning 1967, 1972; Slack and Chrenko 1971; Moore and White 1972; White and Moore 1972; Runciman and Sengupta 1974; Runciman and Marshall 1975; Smith and Langer 1983; Geiger and Rossman 1994; Geiger et al. 2000; Taran et al. 2002, 2007; Khomenko et al. 2002; Krambrock et al. 2013; Platonov and Taran 2018). The spin-allowed electronic transitions of $Fe^{2+}$ for a series of almandine-pyrope and almandine-spessartine solid solutions in the near infrared (NIR) region have been measured and an analysis made using crystal field theory (Geiger and Rossman 1994). Taran et al. (2023) measured the UV/Vis spectra of two different composition almandine bearing and several spessartine-rich garnets and analyzed the spin-forbidden electronic transitions of $Fe^{2+}$ and $Mn^{2+}$, respectively.

Crystal field theory, though a simple physical model, has proved useful in studying crystals with ionic bonding (Burns 1970, 1993). Electronic transitions, both spin-allowed and spin-forbidden, of cations are often interpreted and assigned using theoretical Tanabe-Sugano diagrams that consider cubic, $O_h$, symmetry. The diagrams indicate that the energies of spin-allowed transitions of $Fe^{2+}$, for example, vary much more as a function of local $Fe^{2+}$-O bond lengths (i.e., $Dq$) in different garnet compositions (see Geiger and Rossman 1994) compared to $Fe^{2+}$ spin-forbidden transitions. Indeed, based on theory, most $Fe^{2+}$ and $Mn^{2+}$ spin-forbidden transition energies should be largely independent of garnet composition. However, this has not been investigated and tested experimentally over a range of garnet compositions, for example, across a binary solid solution. In other words, it has not been studied to what degree, if any, the various electronic energies can vary as a function of garnet composition. And if they do, it needs to be determined if they could give information on local cation coordination environments (i.e., $Fe^{2+}$-O and $Mn^{2+}$-O bonding) in a structurally heterogeneous solid solution (see Bosenick et al. 2000; Freeman et al. 2006). In addition, it is not known from theory how spin-forbidden $Fe^{2+}$ and $Mn^{2+}$ transition energies behave under point symmetry $D_2$, as in the triangular dodecahedron of the garnet structure. Semi-empirical calculations of $Fe^{2+}$ transition energies, beyond the level given by simple crystal field and Tanabe-Sugano theory, for garnet are contradictory (i.e., Guo-Yin and Min-Guang 1984; Zhou and Zhao 1984). They also are not in good and full agreement with experimental spectra (Taran et al. 2023). The nature of $Mn^{2+}$ transition energies is even more poorly understood.

Geiger et al. (2003) undertook ab-initio cluster-based electronic-structure calculations to obtain the energies and interpret the spin-allowed $Fe^{2+}$ transitions for various aluminosilicate garnets including binary solid solutions. We are not aware of any recent theoretical or computational studies that give information on spin-forbidden $Fe^{2+}$ and $Mn^{2+}$ transitions and related chemical-bonding properties. In order for calculations to be effective, the existing experimental database (i.e., spectroscopic) has to be as extensive and quantitative as possible. This is presently not the case for most silicate solid-solution systems, and, here, specifically garnet. Thus, careful experimental measurements of spin-forbidden $Fe^{2+}$ and $Mn^{2+}$ energies for a compositionally well-defined binary garnet solid solution are clearly needed.

Considering the various issues, we investigate using UV/Vis single-crystal absorption spectroscopy, the energies of different electronic spin-forbidden bands associated with $Fe^{2+}$ in natural, closely binary almandine-pyrope and $Fe^{2+}$ and $Mn^{2+}$ in natural binary almandine-spessartine solid solutions. The role of $Fe^{3+}$, in nominally $Fe^{3+}$-free almandine-pyrope garnets, is also studied. The electronic energies of spin-forbidden transitions, local crystal-chemical properties and first-order bonding behavior are considered and conclusions drawn.

## Samples and experimental methods: Crystals used for study and UV/Vis spectroscopy

### Samples

The garnets used in this study (as well as for other upcoming works as part of this broad spectroscopic investigation on garnet) from the collections of the authors, Geiger: CAG, Taran: MNT, and Rossman: GRR. Almandine-pyrope garnets are described in Table 1a and almandine-spessartine garnets in Table 1b. The crystals did not show any large deviations from isotropic behavior. The various single crystals, adopted for measurement, were carefully prepared as doubly polished single-crystal platelets of varying thicknesses for spectroscopic and EDS microprobe measurements. Care was used to obtain the necessary crystal thicknesses to record all types of electronic transitions correctly. The garnets, depending on their origin, can have various inclusions, cracks and other "defects," which can complicate the UV/Vis measurements. They can, for example, affect significantly the absorption background of a spectrum through the scattering of light. Clean and transparent areas were selected for study when possible.

### UV/VIS optical absorption single-crystal spectroscopy

In Pasadena, spectra in the wavelength (wavenumber) range between about 380 nm (26 400 $cm^{-1}$) to 1050 nm (9500 $cm^{-1}$) were obtained at about 1.5 nm resolution with a homebuilt microspectrometer. The device contains a 1024 element Si diode-array detector coupled to a 1/3 m grating spectrometer system attached via fiber optics to a highly modified NicPlan infrared microscope. A few spectra were obtained with an older Cary 17I spectrometer system operating at about 1.4 nm resolution that included a photomultiplier tube for the UV/Vis region and a PbS detector for NIR work. Optical spectra were recorded at room temperature and were typically taken on a square area 0.4 to 0.5 mm on a side from a larger crystal.

In Kyiv, spectra were recorded at room temperature using a self-made single-beam microspectrophotometer. It is constructed from a SpectraPro-275 triple grating monochromator and a modified mineralogical microscope, MIN-8, and a PC. Two Ultrafluars 10× objectives served as the objective and condenser in the microscope. The measuring spot was not larger than 200 μm. Two photomultiplier tubes and a PbS cell, cooled by the Peltier effect down to –20 °C, were used as interchangeable photodetectors. The presence of a mechanical, high-stability 300 Hz chopper and lock-in amplifier improve the signal/noise ratio in the 1000–1800 nm (10 000–5556 $cm^{-1}$) range. Stable xenon and quartz-halogen lamps, both with 70 W power, were used as light sources in the ranges 330–450 nm (30 303–22 222 $cm^{-1}$) and 450–1800 nm (22 222–5556 $cm^{-1}$), respectively. The spectra were scanned at steps of $\Delta\lambda$ = 1, 2, and 5 nm in the range 330–450 nm (30 303–22 222 $cm^{-1}$), 450–1000 nm (22 222–10 000 $cm^{-1}$) and 1000–1800 nm (10 000–5556 $cm^{-1}$), respectively. This was done by means of a digital wavelength-step-scanning procedure with an Acton Research Corporation SpectaCard readout system driven by Windows SC-1 control and data-acquisition software.

Band wavenumbers were determined visually by taking the energy at maximum absorption. For the setup in Kyiv, we estimate the uncertainty in the Vis region to be around ±25 $cm^{-1}$ in the case of narrow and well-resolved absorption features. The uncertainty in the energy of weak and broad bands, as well as those that appear as shoulders, is larger. In the UV region, the uncertainty in band energies should also be a little greater.

### Composition determinations

The chemical composition of the different garnets was determined by WDS electron microprobe or single-crystal XRF analysis at Caltech or using a field-

emission scanning electron microscope, model JSM-6700F, equipped with an energy-dispersive spectrometer (EDS), model JED-2300, at the Semenenko Institute in Kyiv. The analyses with the latter were made on carbon-coated garnet platelets that were used for the spectroscopic measurements. The operating conditions were 15 kV accelerating voltage, 0.75 A beam current, 1 μm beam size, and a counting time of 60 s for each point analysis. Elemental Si, Ti, Al, Cr, Fe, Mn, and synthetic MgO and $CaF_2$ were used as standards. The measured raw counts were corrected for matrix effects with the ZAF algorithm implemented by JEOL. Five to seven spots were analyzed per crystal and were averaged to obtain the final composition.

## Results

The chemical analyses showed that the crystals were largely compositionally homogeneous and they did not show any major zoning. The crystal-chemical formulas of the studied garnets are given in Tables 1a and 1b. The various recorded garnet UV/Vis spectra will be shown in the course of the discussion section. However, first, a short interlude into crystal field theory and electronic transitions will be made. The purpose of this is to provide a short theoretical background for this study of $Fe^{2+}$ and $Mn^{2+}$ spin-forbidden transitions for binary almandine-pyrope and almandine-spessartine solid solutions. Our second accompanying work (Taran et al. 2023) involves an analysis on the number, intensities and assignments of $Fe^{2+}$ spin-forbidden transitions in one almandine and one pyrope garnet and $Mn^{2+}$ in several different composition spessartine-rich garnets. Geiger and Taran (2023) consider metal-metal intervalence, i.e., $Fe^{2+} + Fe^{3+} \rightarrow Fe^{3+} + Fe^{2+}$, charge transfer transition for garnets in the system almandine-pyrope-spessartine-grossular. The nature of ligand-metal charge transfer is also discussed in part in Parts II and future work.

## Discussion

### Light absorption, electronic interactions, and UV/Vis spectra of transition-metal-bearing crystals

Optical absorption spectra of minerals containing $3d^N$ transition-metal ions, where N is the number of *d* electrons, can show electronic absorption bands of three main types. They can occur in the UV, Vis, and NIR spectral regions. They are: (1) crystal-field or *dd*-transition bands; (2) charge-transfer bands of the ligand-metal and metal-metal type; and (3) bands of exchange-coupled $3d^N$-ion pairs. We discuss them briefly. A more complete treatment can be found in Marfunin (1979) and Burns (1970, 1993).

**Crystal-field or *d-d* electronic transitions.** They are frequently observed in the spectra of minerals and have received much study, both experimental and theoretical. They are caused by electronic transitions between partly filled *d* orbitals of transition metal ions, and they are often interpreted using crystal field theory (e.g., Marfunin 1979; Burns 1970, 1993). This theory describes the electronic interactions in a chromophore complex, for example, consisting of a central transition metal ion and the nearest surrounding ligands. The interaction between the negatively charged ligands and the positively charged central atom is assumed to be purely electrostatic. The metal atom resides in an electric field of a certain intensity and symmetry as caused by the nearest surrounding ligands whose precise electronic structure is ignored. The latter is regarded as structure-less point charges (or sometimes as dipoles) having an outer electrostatic field. The crystal field strength, *Dq*, of a metal-ligand bond is given by:

$$10Dq = \frac{5\langle r^4 \rangle (Z_L e^2)}{3\overline{R}^5} \quad (1)$$

where $\overline{R}$ is the mean metal-ligand distance, $\langle r^4 \rangle$ is the mean value to the fourth power of the radial distance of a 3*d* orbital from the nucleus, and $(Z_L e^2)$ is the charge on the ligands. The numerator is assumed to be approximately constant for cations of similar valence within the same transition series. With increasing *R*, the influence of other ions not belonging to the main coordination polyhedron is considered small and, in most cases, is neglected.

The ligand field acting on a central ion causes a splitting of the electronic energy levels of the $3d^N$ ion, which are degenerate in the free spherically symmetrical state. The splitting is a function of the degree of deviation of the local symmetry from a spherical one due to the immediate surrounding crystal field. Electronic transitions from the lowest energy level (i.e., the ground state) to higher energy levels (i.e., excited states) result from the absorption of a quantum of electromagnetic radiation of a given energy. The energy of a transition is given by a band in an experimental optical absorption spectrum. Thus, optical spectra give information on the electronic structure of a $3d^N$ ion in a local crystal field.

In accordance with Hund's rule, the ground electronic state has the largest spin multiplicity, *S*, for a given $3d^N$ electronic configuration. There are spin-allowed (i.e., $\Delta S = 0$) and/or spin-forbidden (i.e., $\Delta S \neq 0$) transitions depending on the difference in spin multiplicities of the electronic states involved in a transition. The former bands are typically broad and intense with an oscillator strength of $f = 10^{-4}$ to $10^{-5}$. The latter are three to four orders of magnitude weaker and tend to be narrow in breadth. They can occur on or overlap other more intense electronic bands. The energy and broadness of both spin-allowed and spin-forbidden bands can be analyzed using Tanabe-Sugano diagrams in the approximation of local cubic symmetry, namely $O_h$ (e.g., Burns 1993). In the case of lower symmetry, as is typical for many mineral structures, degenerate electronic levels split further. Here, Tanabe-Sugano diagrams are more difficult to apply and the interpretation of the spectra can be considerably more complicated [see Taran et al. (2023) for the case of spessartine].

It should be noted that crystal field theory (CFT) is incomplete in the sense that it treats the ligands surrounding a metal cation as simple point charges. Covalent bonding properties are not accounted for as in ligand field theory. Only the *d* orbitals of the metals are considered and not those of the *s* and *p* orbitals or the orbitals of the ligands. In terms of silicates, CFT has, though, been used successfully, because the bonding between transition metals and oxygen is largely ionic. Charge-transfer transitions, as discussed next, are also not treated by CFT.

**Charge-transfer transitions.** They can affect color, pleochroism and other spectroscopic properties of $3d^N$-ion-bearing minerals. They are subdivided into two different types: charge-transfer (CT) ligand-metal (L → M) and metal-metal (M → M) electronic transitions. The absorption bands related to the former are governed by Laporte or parity selection rules between bonding and anti-bonding molecular orbitals in a transition-metal-ligand coordination cluster, for example. The molecular orbitals are localized on the different atoms, both ligands and

**TABLE 1a.** List and description of various natural and synthetic almandine-pyrope garnets (only those samples listed in Online Materials[1] Table OM1a were considered in the analysis of this work)

| Garnet species and sample label | Locality/synthesis conditions | Sample description | Composition |
|---|---|---|---|
| Synthetic Almandine A-2 | $P(H_2O)$ = 15 kbar, $T$ = 800 °C in iron capsule 24 h | 0.5–1 mm crystals, dark pink to red; Geiger and Rossman (1994) | $Fe_{3.00}[Al_{1.91}Fe^{3+}_{0.09}]Si_{3.00}O_{12}$ |
| Almandine FR-3 | near Collobrières, France | 0.24 mm, Metamorphosed ironstone; Woodland et al. (1995); Dachs et al. (2012) | $(Fe_{2.83}Mg_{0.07}Ca_{0.09})[Al_{1.92}Fe^{3+}_{0.08}]Si_{2.99}O_{12}$ |
| Almandine A-5 | near Collobrières, France | 0.216 mm, MNHN 6956 (V); Pinet and Smith (1994); Geiger and Rossman (1994) | $(Fe_{2.82}Mg_{0.03}Mn_{0.04}Ca_{0.16})[Al_{2.05}Ti^{4+}_{0.01}]Si_{2.96}O_{12}$ |
| Almandine JF-1 | Zlaty Chlum near Jesenik, Czech Republic | 0.50 mm, Aparicio et al. (2012); Geiger and Rossman (2018) | $(Fe_{2.85}Mg_{0.11}Mn_{0.02}Ca_{0.05})Al_{1.99}Si_{2.99}O_{12}$ |
| Almandine GRR 3276 | India (?) | 0.213 mm, Faceted dark purplish red gem; unknown jewelry dealer | $(Fe_{2.5}Mg_{0.3}Mn_{0.1}Ca_{0.1})Al_{2.0}Si_{3.0}O_{12}$ |
| Almandine A-12 | Velusina, Macedonia | MNHN (V); Pinet and Smith (1994); Geiger and Rossman (1994) | $(Fe_{2.36}Mg_{0.50}Mn_{0.03}Ca_{0.07})Al_{2.10}Si_{2.95}O_{12}$ |
| Almandine A-13 | Portugal | 0.71 mm, MNHN (V); Pinet and Smith (1994); Geiger and Rossman (1994) | $(Fe_{2.40}Mg_{0.26}Mn_{0.24}Ca_{0.06})Al_{2.07}Si_{2.96}O_{12}$ |
| Almandine Jai-1 | Jaipur, India | 1.44 mm, Geiger and Rossman (1994) | $(Fe_{2.29}Mg_{0.73}Mn_{0.02}Ca_{0.03})Al_{2.01}Si_{2.96}O_{12}$ |
| Almandine GRR 1040 | North River, New York, U.S.A. | 1.54 mm, deep reddish-purple slab; W.C. Oke collection Geiger and Rossman (1994) | $(Fe_{1.35}Mg_{1.30}Mn_{0.03}Ca_{0.26})Al_{1.99}Si_{3.01}O_{12}$ |
| Almandine GRR 1056 | Wrangell, Arkansas, U.S.A. | 1.10 mm; reddish-purple slab; Caltech reference collection Pabst (1943); Bressler (1945/1946); Geiger and Rossman (1994) | $(Fe_{2.03}Mg_{0.67}Ca_{0.18}Mn_{0.07})Al_{2.00}Si_{3.00}O_{12}$ |
| Almandine Lind 3 | Rajasthan, India | 1.06 mm, H. Lind | $(Fe_{2.05}Mg_{0.91}Ca_{0.03})[Al_{2.00}Fe^{3+}_{0.02}Ti_{0.01}]Si_{2.99}O_{12}$ |
| Almandine GTF 90-28 | Wrangell, Arkansas, U.S.A. | 0.56 mm, Pabst (1943); Bressler (1945/1946) | $(Fe_{2.13}Mg_{0.66}Ca_{0.14}Mn_{0.05})Al_{1.94}Si_{3.00}O_{12}$ |
| Pyrope GRR 750 | Zircon Point, Casey Bay, Enderby Land, Antarctica | E. Grew; Geiger and Rossman (1994) | $(Fe_{1.71}Mg_{1.25}Ca_{0.09}Mn_{0.02})Al_{2.04}Si_{2.97}O_{12}$ |
| Pyrope GTF 90-33 | De Luca pit, Emery Hill, Cortlandt, New York, U.S.A. | 0.30 mm, orange-pink; hornfels; Taran et al. (2007) | $(Mg_{1.33}Fe_{1.29}Ca_{0.20}Mn_{0.06})[Al_{1.96}Fe^{3+}_{0.10}]Si_{2.99}Al_{0.01}O_{12}$ |
| Pyrope SM 1597 | Cowee Valley, North Carolina, U.S.A. | 0.55 mm, rhodolite; A. Hofmeister; Taran et al. (2007) | $(Fe_{1.18}Mg_{1.70}Ca_{0.07}Mn_{0.04})[Al_{1.97}Ti_{0.01}]Si_{3.01}O_{12}$ |
| Pyrope 200924473845 | Africa | 0.94 mm, 2.15 carat cut crystal, eBay, labeled "Almandine" | $(Fe_{1.18}Mg_{1.56}Ca_{0.25}Mn_{0.01})[Al_{1.92}Fe^{3+}_{0.08}]Si_{2.99}O_{12}$ |
| Pyrope 200924659028 | Africa | 1.40 mm, cut crystal, eBay, labeled "Almandine" | $(Fe_{1.16}Mg_{1.45}Ca_{0.34}Mn_{0.05})[Al_{1.97}Fe^{3+}_{0.03}]Si_{2.99}O_{12}$ |
| Pyrope 200939608981 | Africa | 0.97 mm, dark red, cut crystal, eBay, labeled "Almandine" | $(Fe_{1.18}Mg_{1.47}Ca_{0.31}Mn_{0.04})[Al_{2.00}]Si_{3.00}O_{12}$ |
| Pyrope 17405755 | Rakwana mining area, Ratnapura area, Sri Lanka | 3.49 mm, GIA, A. Rajamanickam/ V. Pardieu | $(Fe_{1.14}Mg_{1.75}Ca_{0.11}Mn_{0.01})[Al_{1.91}Fe^{3+}_{0.09}]Si_{3.00}O_{12}$ |
| Pyrope GRR 749b | Anakapalle, Andhra Pradesh, India | 1.09 mm, E. Grew; Geiger and Rossman (1994) | $(Mg_{1.69}Fe_{1.21}Ca_{0.08}Mn_{0.02})[Al_{1.99}Fe^{3+}_{0.03}]Si_{2.98}O_{12}$—EMP |
| Pyrope GRR 131 | unknown locality, East Africa Tanzania(?) | 2.007 mm, Caltech Seismological Lab; Geiger and Rossman (1994) | $(Mg_{1.82}Fe_{0.98}Ca_{0.16}Mn_{0.04})Al_{2.00}Si_{2.99}O_{12}$—EMP |
| Pyrope P-10 | Ambodirafia, Madagascar | 1.00 mm, MNHN 119.32; Geiger and Rossman (1994) | $(Mg_{1.47}Fe_{1.43}Mn_{0.02}Ca_{0.05})[Al_{2.12}Cr_{0.01}]Si_{2.96}O_{12}$ |
| Pyrope GRR 779 | Umba River Valley, Tanzania | 0.79 mm, variety rhodolite; P. Flusser, Overland Gems; Geiger and Rossman (1994) | $(Mg_{1.61}Fe_{1.22}Mn_{0.04}Ca_{0.14})Al_{2.01}Si_{2.97}O_{12}$ |
| Pyrope GRR 892 | Himalaya Mountains, Nepal | A. Boettcher | $(Mg_{1.67}Fe_{1.14}Ca_{0.11})Al_{1.92}Si_{2.97}O_{12}$—XRF |
| Pyrope 9093 | Madagascar | 1.06 mm, rhodolite; eBay | $(Fe_{1.08}Mg_{1.76}Ca_{0.11}Mn_{0.05})[Al_{1.92}Fe^{3+}_{0.08}Cr_{0.01}]Si_{3.00}O_{12}$ |
| Pyrope 39060255315 | Africa | 1.56 mm, cut stone, eBay, labeled "Spessartine-Almandine" | $(Fe_{1.00}Mg_{1.75}Ca_{0.24}Mn_{0.02})[Al_{1.93}Fe^{3+}_{0.07}Ti_{0.01}]Si_{2.99}O_{12}$ |
| Pyrope GRR 2268 | Madagascar | 1.54 mm, faceted gem, variety rhodolite; N. Brewer | $(Mg_{1.75}Fe_{1.04}Ca_{0.13}Mn_{0.06})Al_{1.98}Si_{3.01}O_{12}$ |
| Pyrope GRR 2351 | Kuranze—Kwale District Kenya | 0.79 mm, rhodolite; J. Clanin | $(Mg_{1.77}Fe_{1.24}Mn_{0.03}Ca_{0.11})Al_{1.97}Si_{3.00}O_{12}$—XRF |
| Pyrope GRR 83 | Tanzania | 0.78 mm, rhodolite; Pala International, Geiger and Rossman (1994) | $(Mg_{2.09}Fe_{0.78}Mn_{0.11}Ca_{0.11})[Al_{1.97}Cr_{0.02}]Si_{2.97}O_{12}$ |
| Pyrope GRR 86 | Tanzania | 1.71 mm, rhodolite; Pala International | $(Mg_{1.1}Fe_{1.8}Mn_{0.07}Ca_{0.17})Al_{1.95}Si_{2.98}O_{12}$—XRF |
| Pyrope 17405762 | Turtle Land mine, Torapitiya area, Sri Lanka | 4.32 mm, rhodolite; GIA, A. Konara/V. Pardieu | $(Mg_{2.19}Fe_{0.69}Ca_{0.13})[Al_{1.90}Fe^{3+}_{0.08}Cr_{0.01}Ti_{0.01}]Si_{3.00}O_{12}$ |
| Pyrope 17405757 | Rakwana mining area, Ratnapura area, Sri Lanka | 2.95 mm, GIA, A. Rajamanickam/V. Pardieu | $(Mg_{2.12}Fe_{0.73}Ca_{0.11}Mn_{0.05})[Al_{1.90}Fe^{3+}_{0.09}Ti_{0.01}]Si_{3.00}O_{12}$ |
| Pyrope 17405751 | Gold mining area, Ruvu River, Matombo area, Tanzania | 3.18 mm, GIA, V. Pardieu | $(Mg_{2.10}Fe_{0.67}Mn_{0.14}Ca_{0.10})[Al_{1.93}Fe^{3+}_{0.07}Cr_{0.01}]Si_{3.00}O_{12}$ |
| Pyrope 17405770 | Turtle Land mine, Torapitiya area, Sri Lanka | 2.21 mm, rhodolite; GIA, A. Konara/V. Pardieu | $(Mg_{2.22}Fe_{0.65}Ca_{0.13})[Al_{1.86}Fe^{3+}_{0.12}Cr_{0.01}]Si_{3.00}O_{12}$ |
| Pyrope SB 1 | San Bernardo, Dora Maira, Italy | 2.07 mm, light pink, Geiger and Rossman (1994, 2018) | $(Mg_{2.59}Fe_{0.35}Ca_{0.07})[Al_{1.97}Cr_{0.01}]Si_{3.01}O_{12}$ |
| Pyrope SB 2 | San Bernardo, Dora Maira, Italy | 3.69 mm, dark pink, Geiger and Rossman (1994, 2018) | $(Mg_{2.54}Fe_{0.36}Ca_{0.09})[Al_{1.96}Fe^{3+}_{0.05}Cr_{0.01}]Si_{2.99}O_{12}$ |
| Pyrope | Precise locality unknown, Dora Maira, Italy | 2.96 mm, colorless, Geiger and Rossman (1994, 2018) | $(Mg_{2.95}Fe_{0.04}Mn_{0.01}Ca_{0.01})[Al_{1.99}Ti_{0.01}]Si_{2.99}O_{12}$ |

**TABLE 1b.** List and description of various natural almandine-spessartine garnets (only those samples listed in Online Materials[1] Table OM1b were considered in the analysis of this work)

| Garnet species and sample label | Locality | Sample description | Composition |
|---|---|---|---|
| Almandine A-3 | Roscoff, Sierck, Morbihan, France | 0.75; MNHN (V), Pinet and Smith (1994); Geiger and Rossman (1994) | $(Fe_{2.06}Mn_{0.76}Mg_{0.08}Ca_{0.02})[Al_{2.05}Ti^{4+}_{0.01}]Si_{2.96}O_{12}$ |
| Almandine A-20 | Caladroy, Pyrénées-Orientales, France | 1.01 mm; MNHN (V) 2448A; Pinet and Smith (1994); Geiger and Rossman (1994) | $(Fe_{2.11}Mn_{0.77}Mg_{0.08}Ca_{0.02})Al_{2.06}Si_{2.96}O_{12}$ |
| Almandine GRR 3276 | India(?) | 0.50 and 0.213 mm; faceted dark purplish red gem; unknown jewelry dealer | $(Fe_{2.5}Mg_{0.3}Mn_{0.1}Ca_{0.1})Al_{2.0}Si_{3.0}O_{12}$ |
| Almandine GRR 141 | East Africa? | 1.333 mm; vivid purplish red, E. Gaffney, Caltech Shockwave Lab; Geiger and Rossman (1994) | $(Fe_{1.42}Mn_{1.36}Ca_{0.03})Al_{2.01}Si_{2.99}O_{12}$ |
| Almandine GRR 943 | San Jacinto Mtn, Riverside County, California, U.S.A. | 2.70 mm; R. Hill, Caltech collection CIT-9968; Geiger and Rossman (1994) | $(Fe_{2.43}Ca_{0.16}Mn_{0.21}Mg_{0.09})Al_{2.01}Si_{3.00}O_{12}$ |
| Spessartine Lind 2 | Namibia | 0.50 mm; Sps-Pyp, H. Lind | $(Mn_{2.44}Fe_{0.14}Mg_{0.37}Ca_{0.04})[Al_{1.99}Fe_{0.01}Ti_{0.01}]Si_{2.99}O_{12}$ |
| Spessartine GRR 59b | Tanzania | Deep orange; Caltech Shockwave Lab; Geiger and Rossman (1994) | $(Mn_{1.72}Fe_{1.22}Ca_{0.02}Mg_{0.01})Al_{2.01}Si_{3.00}O_{12}$ |
| Spessartine GRR 61 | Brazil | 1.35 mm; deep purplish red; Caltech Shockwave Lab; Geiger and Rossman (1994) | $(Mn_{1.56}Fe_{1.38}Ca_{0.02})Al_{2.00}Si_{3.01}O_{12}$ |
| Spessartine GRR 1052 | Broken Hill, NSW, Australia | 0.884 mm; deep reddish purple; Caltech collection CIT-11826 | $(Mn_{2.04}Fe_{0.63}Ca_{0.37})[Al_{1.89}Fe_{0.13}Ti_{0.01}]Si_{2.99}O_{12}$—XRF |
| Spessartine GRR 31 | Minas Gerais, Brazil | 0.905 mm; light orange; Caltech reference collection CIT-7765 | $(Mn_{2.87}Fe_{0.10})Al_{1.96}Si_{3.00}O_{12}$—XRF |
| Spessartine GRR 44B | Amelia, Virginia, U.S.A. | 1.192 mm; grayish purplish red; Caltech collection CIT-6725 | $(Mn_{1.99}Fe_{0.88}Ca_{0.16})Al_{2.03}Si_{2.97}O_{12}$ |
| Spessartine GRR 1018 | Rincon District, San Diego Co., California, U.S.A. | 1.145 mm; pegmatite district, Caltech collection CIT-15008; Geiger and Rossman (1994) | $(Mn_{1.35}Fe_{1.34}Mg_{0.09}Ca_{0.01})Al_{2.01}Si_{3.09}O_{12}$ |
| Spessartine GRR 1041 | Spruce Spine District, North Carolina, U.S.A. | 0.752 mm; dark reddish orange; Pegmatite, Caltech collection CIT-1738; Swanson and Veal (2010) | $(Mn_{1.64}Fe_{1.12}Mg_{0.03}Ca_{0.10})[Al_{1.95}Fe^{3+}_{0.05}]Si_{3.08}O_{12}$ |
| Spessartine GRR 942 | Ramona, California, U.S.A. | 0.696 mm; deep orange; M. Gray | $(Mn_{2.72}Fe_{0.24})Al_{1.98}Si_{3.00}O_{12}$—XRF |
| Spessartine S-7 | Chanteloube, Haute Vienne, France | MNHN (V), Pinet and Smith (1994) | $(Mn_{1.52}Fe_{1.44}Mg_{0.01}Ca_{0.02})Al_{1.98}Si_{3.00}O_{12}$—XRF |
| Spessartine 37092827 1669 (316306) | Africa? | 0.67 and 0.25 mm; cut crystal, ThaiGemStore; eBay | $(Mn_{2.30}Fe_{0.47}Mg_{0.15}Ca_{0.09})[Al_{1.97}Fe^{3+}_{0.02}Ti_{0.01}]$ $Si_{3.00}O_{12}$—EDS |
| Spessartine S-14 | Brasil | MNHN (V), Pinet and Smith (1994) | $(Mn_{1.86}Fe_{1.07}Ca_{0.06})Al_{2.00}Si_{3.00}O_{12}$ |
| Spessartine GRR 2956 | Little 3 Mine, near Ramona, San Diego Co.,California, U.S.A. | 0.51 mm; M. Evans, GIA, 3 to 5 mm crystals | $(Mn_{2.52}Fe_{0.45}\ Ca_{0.01})[Al_{2.03}Fe^{3+}_{0.01}]Si_{2.98}O_{12}$—EDS |
| Spessartine GRR 72 | Minas Gerais, Brazil | 1.365 mm; purchased from Grieger's | $(Mn_{2.79}Fe_{0.07}Mg_{0.04}Ca_{0.08})Al_{2.06}Si_{3.05}O_{12}$ |
| Spessartine GRR 43 | Amelia, Virginia, U.S.A. | 0.858 mm; light orange, Caltech collection | $(Mn_{2.82}Fe_{0.10})Al_{2.02}Si_{3.00}O_{12}$—XRF |
| Spessartine MMUR 32999/912 | Wushan Spessartine Mine, Fujian Province, PR. China | 0.472 mm; orange, Boiocchi et al. (2012) | $\{Mn^{2+}_{2.87}Fe^{2+}_{0.09}Ca_{0.04}\}[Al_{1.94}Fe^{3+}_{0.06}](SiO_4)_{2.52}$ $(OH_{1.11},F_{0.81})$ |
| Spessartine S-18 | Tsilaisina, Madagascar | 1.54 mm; MNHN 111.456; Pinet and Smith (1994) | $(Mn_{2.88}Fe_{0.04}Ca_{0.06})[Al_{1.95}Fe^{3+}_{0.05}]Si_{3.00}O_{12}$ |

*Note:* MNHM = Muséum National d'Histoire Naturelle (V = Vésignié), Paris; GIA = Gemological Institute of America.

the central cation, and the electronic transitions are accompanied by a transfer of charge from the former to the latter. Because the L → M charge-transfer transition is allowed by parity selection rules, they are extremely intense with values of $f = 1$ to $10^{-1}$. Their spectroscopic band maxima are typically located in the high-energy UV range of the electromagnetic spectrum. They are manifested in a typical optical absorption spectrum by their low-energy absorption edge or flank that can extend down into the visible range. Thereby, color can be affected. Because L → M charge-transfer bands are so intense (i.e., their bands are difficult to record on scale) and because they occur mostly in the UV region, they have received little study in minerals.

Electronic M → M CT transitions can appear in the spectra of various oxides and silicates containing $3d^N$ ions that have different formal valence states. For example, minerals containing $Fe^{2+}$ and $Fe^{3+}$ can display intense coloration. The interaction involves the transfer of electronic density from the donor (e.g., $Fe^{2+}$) to the acceptor (e.g., $Fe^{3+}$) and it leads to electronic delocalization. In several $Fe^{2+}$- and $Fe^{3+}$-bearing oxides and silicates, for example, this interaction can give rise to a broad intense band between ~11 000 and ~18 000 $cm^{-1}$. In garnet, this type of transition occurs at higher energies around 21 000–22 000 $cm^{-1}$ (Taran et al. 2007). In anisotropic crystals, these bands are polarized and they give rise to pleochroism. Heteronuclear IVCT transitions ($Fe^{2+} + Ti^{4+} \rightarrow Fe^{3+} + Ti^{3+}$) can also occur and their broad intense absorption bands typically lie at higher energies between 20 000 and 24 000 $cm^{-1}$.

**Exchange-coupled transitions related to local pairing of $3d^N$ ions.** An electronic exchange interaction between $3d^N$ ions may not necessarily lead to IVCT absorption bands in UV/Vis spectra, but it can cause an increase in the intensity of both spin-allowed and spin-forbidden crystal-field transitions.

## Almandine and spessartine crystal chemistry

The garnet crystal structure is shown in Figure 1a. Local structural relationships between neighboring octahedra and dodecahedra, which contain transitions metals (i.e., for aluminosilicate garnets), are illustrated as well (Figs. 1b, 1c, and 1d). Common rock-forming garnet can contain $Fe^{2+,3+}$, $Cr^{3+}$, $Mn^{2+,3+}$, $V^{3+}$, and $Ti^{4+}$ at major to minor concentrations depending on the garnet species and the petrologic occurrence.

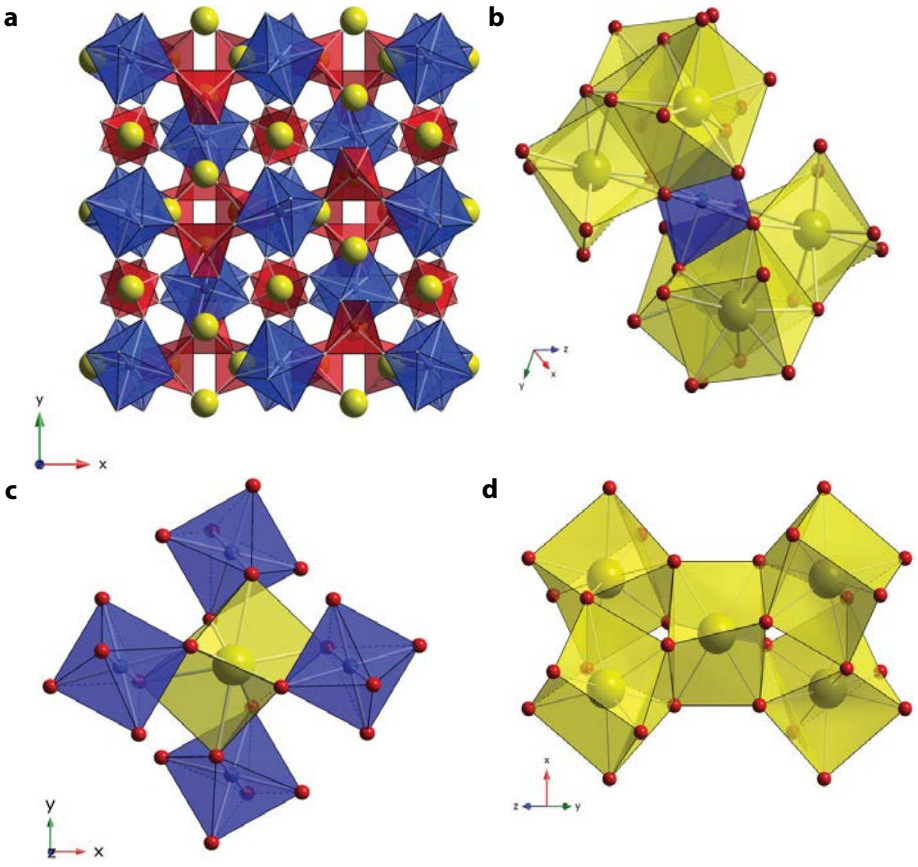


**Figure 1.** (**a**) Polyhedral structure model of garnet. The tetrahedra and octahedra are connected via shared corners and build a three-dimensional quasi framework. The $X^{2+}$ cations (yellow spheres) are located in small cavities of triangular dodecahedral coordination. The small red spheres are oxygen ions and they lie on a single general crystallographic position *x*, *y*, *z*. (**b**) A central octahedron and six edge-shared dodecahedra (the polyhedral faces are shown as concave to make the visualizing easier). (**c**) A central triangular dodecahedron and four edge-shared octahedra. (**d**) Edge-sharing relationship between neighboring triangular dodecahedra. (Color online.)

Most almandines contain (aside from $Fe^{2+}$), in general, major to minor $Mn^{2+}$, minor $Fe^{3+}$, and $Ti^{4+}$ (Deer et al. 1982), while $Mn^{3+}$, $Cr^{3+}$, and $V^{3+}$ range from being minor to trace in concentration. Cr concentrations between about 30 and 1000 ppm were measured for compositionally zoned garnets from pelitic schists, for example, by Schwandt et al. (1996). V concentrations were roughly between about 15 and 1000 ppm. Hickmott et al. (1987) measured roughly 300 ppm Cr and much less V in garnet from an amphibolite from the Tauern Window, Austria. Čopjaková et al. (2005) measured Cr and V concentrations mostly below 250 ppm for different almandine garnets sampled from sediments. In summary, the amount of these two elements can vary, but it appears that they typically show concentrations from tens to a couple of several hundreds of parts per million in most almandines. The amounts of $Mn^{3+}$ are not known.

Many spessartines can be described well by the system spessartine-almandine with lesser amounts of pyrope and grossular components (Deer et al. 1982), but more unusual compositions have been documented. Some spessartines can show more chemical variability than almandine-rich crystals. Less research has been done on measuring different minor and trace elements in spessartine compared to almandine or pyrope. That said, there is a class of spessartine-pyrope garnets that contain small amounts of $V_2O_3$ (0.09–0.68 wt%) and $Cr_2O_3$ [0.04–0.63 wt%; see Manson and Stockton (1984) for these results but see also Schmetzer et al. (2001)]. These transition metals can affect markedly the color of these crystals. There is also a class of seldom occurring spessartine-andradite rich garnets (see Korinevsky 2015). The spessartine-almandine garnets studied here (Table 1b) do not appear to have significant amounts of $V_2O_3$ and $Cr_2O_3$, so as to give rise to absorption bands in the visible region. Any possible $Fe_2O_3$ in spessartine is not thought to affect the results of this study. It may, though, play a role in affecting the nature of the O → M CT edge [Taran et al. (2023) and upcoming work] as could possibly $TiO_2$ as well.

Based on current crystal chemical understanding of "lower pressure" aluminosilicate garnets and with regard to the behavior of transition metals cations, the triangular dodecahedrally coordinated X cation is $Fe^{2+}$ and/or $Mn^{2+}$. Trivalent and tetravalent charged transition-metal cations are mostly (or exclusively) located at the octahedral site.

## Spectral analysis

As discussed above, various electronic transitions can occur in crystals and silicate garnet is an interesting system for studying them. We focus our analysis in this investigation on the spin-forbidden transitions relating to $Fe^{2+}$ and $Mn^{2+}$. $Fe^{3+}$ is also considered as it can occur in small amounts in many garnets. Our approach is a first-order experimental one and empirical. We focus our attention on energy behavior of different electronic transitions as a function of garnet composition. Taran et al. (2023) and upcoming work focus on the physical nature of different absorption features and their spectroscopic assignments.

### Spectra of almandine-pyrope solid solutions

The early experimental investigations of Moore and White (1972) and White and Moore (1972) provide a good starting point in the study of $Fe^{2+}$, $Mn^{2+}$, and $Fe^{3+}$ electronic transitions in garnets of different composition. They measured the UV/Vis/NIR spectra of several silicate garnets, including various composition almandines, pyropes and spessartines and concentrated their investigation on the crystal field electronic absorption bands. Unfortunately, full spectra for many of their studied garnets are not shown. They labeled their observed electronic absorption transitions with increasing energy with the letters a to c for $Fe^{2+}$ spin-allowed bands and d to r for the various $Fe^{2+}$, $Mn^{2+}$, and $Fe^{3+}$ spin-forbidden bands. The energies of the spin-forbidden bands d to r bands are given for all their samples in Moore and White (1972). Taran et al. (2023) measured the spectra of an almandine and an almandine-bearing pyrope and analyzed further the different $Fe^{2+}$ and $Fe^{3+}$ transitions that can occur. A couple of absorption features that were not noted by Moore and White (1972) and/or possibly incorrectly assigned are discussed in the former work and the results of the latter workers are partly modified. Taran et al. (2023) also give an up-to-date analysis on the assignments for the spin-forbidden bands of $Fe^{2+}$, $Mn^{2+}$, and $Fe^{3+}$.

**Energy behavior of spin-forbidden $Fe^{2+}$ transitions.** We measured the UV/Vis single-crystal spectra for several natural garnets belonging to the almandine-pyrope solid solution. The amounts of Ca and $Mn^{2+}$ are, in general, low (Table 1a). Figure 2 shows a stacked plot of UV/Vis absorption spectra of eight representative garnets with different $Fe^{2+}/(Fe^{2+} + Mg)$ ratios. Several spin-forbidden absorption bands can be observed. We consider those related to $^{VIII}Fe^{2+}$ first. Bands d to h are observed in most spectra and f, g, and h are the most intense. Bands d, e, f, and g are broader than the higher wavenumber bands. Band i is expressed as a weak high-energy shoulder on the intense band h. Band j* needs special comment. It is observed as a weak poorly defined absorption feature in some of the almandine-pyrope garnet spectra. Moore and White (1972) assigned it to a spin-forbidden band of $Mn^{2+}$. However, it can be observed in spectra of some garnets with no measurable $Mn^{2+}$. In addition, it can be obtained in spectral deconvolutions of almandine and pyrope-almandine garnets (Taran et al. 2023). This weak feature could, therefore, be related to a $Fe^{2+}$ transition. Bands k and q appear to be weaker in intensity than bands d to g and are best observed in the spectra of almandine-rich garnets. A few almandine spectra (e.g., GRR 3256) appear to show a weak shoulder on the high-energy edge of band k. Finally, there appears to be a weak spectral feature occurring between band m and q at about 24 200–24 300 $cm^{-1}$ [see Taran et al. (2023) for further discussion on modified and more complete band labels and assignments]. Because we observe this weak feature in the spectra of garnets with no measurable $Mn^{2+}$, we think, once again, it is best assigned to $Fe^{2+}$.

Online Materials[1] Table OM1a lists the wavenumbers of various $Fe^{2+}$ spin-forbidden bands, as based on an analysis of their peak maxima, as far as this is possible (e.g., energies for band i are estimates) for the different almandine-pyrope garnets studied herein (Table 1a). The results agree to first order with previously published values. The energy behavior of these bands is shown in Figure 3 as a function of almandine content in the solid-solution crystals. Bands d, e, and f decrease slightly in energy, <125 $cm^{-1}$, with increasing pyrope component across the join. Bands h, i, and k, in contrast, increase slightly in energy between about 80 to 150 $cm^{-1}$ with increasing pyrope component. The highest wavenumber band q increases the most in energy (~325 $cm^{-1}$) going from nearly end-member almandine to nearly end-member pyrope.

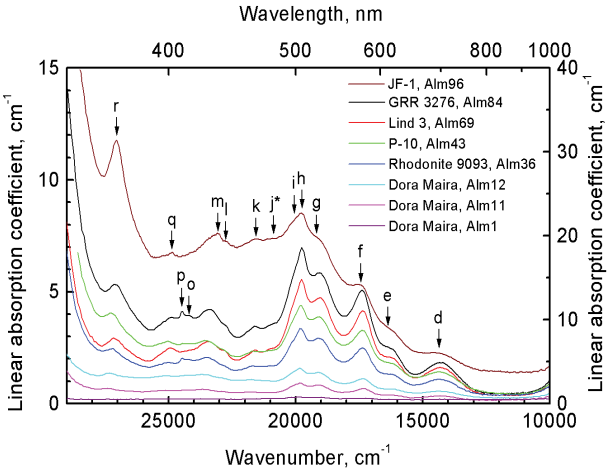


**Figure 2.** Stacked plot of eight almandine-pyrope garnet spectra with increasing almandine content from bottom to top. The arrows indicate various spin-forbidden bands. The letters follow the labeling of Moore and White (1972), as slightly modified by Taran et al. (2023). The weak bands labeled p and o are related to $Mn^{2+}$ and bands l, m, and r are related to $Fe^{3+}$. All other bands are due to $Fe^{2+}$. The "baseline" absorption increases with increasing amandine (and $Fe^{3+}$) in the garnet because the O → M CT tail extends into the visible region. The spectrum of almandine JF-1 (whose absorption is given by the ordinate on the right) probably indicates the presence of a broad $^{VIII}Fe^{2+} + {}^{VI}Fe^{3+} \rightarrow {}^{VIII}Fe^{3+} + {}^{VI}Fe^{2+}$ IVCT band centered roughly at 22 000 $cm^{-1}$ (Geiger and Taran 2023). Its background is also especially high because of the presence of numerous tiny solid inclusions scattered throughout the crystal. (Color online.)

**Energy behavior of spin-forbidden $Fe^{3+}$ transitions.** Moore and White (1972) assigned the three bands l, m and r to electronic transitions of $Fe^{3+}$ located at the octahedral site of garnet. These bands can be observed in the spectra of many almandine-pyrope garnets, especially band r, which is the most intense of the three (Fig. 2). Their energy behavior as a function of almandine content is shown in Figure 3. All three bands appear to increase in energy from near-end-member almandine to near end-member pyrope especially bands m and r.

### Spectra of almandine-spessartine solid solutions

The UV/Vis spectroscopic investigations of Moore and White (1972), Smith and Langer (1983), and Taran et al. (2023) provide a starting point for the analysis of our spectra of almandine-spessartine solid-solutions (Table 1b). The amounts of Ca and $Mg^{2+}$ are, in general, low, but a couple of crystals have more extended compositions and are best described as pyrope-almandine-spessartine garnets (e.g., GRR 83). Figure 4 shows a stacked plot of seven UV/Vis absorption spectra for garnets with different spessartine contents. The intent is to primarily document the behavior of the most narrow and intense $Mn^{2+}$ spin-forbidden bands located between 23 000 and 25 000 $cm^{-1}$.

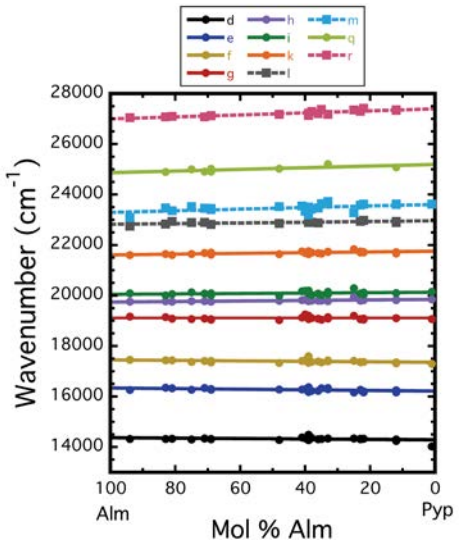


**Figure 3.** Energies for various spin-forbidden bands related to $Fe^{2+}$ (solid circles) and $Fe^{3+}$ (solid squares) as a function of almandine mole percent (Online Materials[1] Table OM1a) for almandine-pyrope solid solutions. The size of the symbols is larger than the experimental uncertainty. The letters describe the various bands following Moore and White (1972), as modified by this work and Taran et al. (2023). The lines represent linear least-squares best fits to the energies of the different bands. (Color online.)

We consider the energies of the $Fe^{2+}$ electronic transitions first.

**Energy of spin-forbidden $Fe^{2+}$ transitions.** Online Materials[1] Table OM1b lists the various $Fe^{2+}$ absorption bands and their wavenumbers for the studied almandine-spessartine garnets. The wavenumbers are plotted as a function of almandine content in Figure 5. The lowest wavenumber bands d, e, and f increase in energy between 300 to 425 $cm^{-1}$ with increasing spessartine component across the join. Bands g, h, i, and k show less change in energy across the binary. The energies of bands h and k do not vary significantly, band g may decrease slightly and band i may increase with increasing spessartine in the garnet, but these variations may be within the level of experimental uncertainty. Band q, which is weak in intensity, was not recorded in many spectra and, therefore, is not considered.

**Energy of spin-forbidden $Mn^{2+}$ transitions.** Online Materials[1] Table OM1b lists several $Mn^{2+}$ absorption bands and their wavenumbers for several the studied almandine-spessartine garnets (Table 1b). Only the energies of the bands that could be determined with some degree of precision are listed and they are the four relatively intense narrow ones located between 23 000 and 25 000 $cm^{-1}$. Lower wavenumber $Mn^{2+}$ bands (Taran et al. 2023) are weaker in intensity and broader and are, therefore, not considered. Figure 6 shows the energy behavior of these $Mn^{2+}$ spin-forbidden bands as a function of spessartine component in the garnet. A simple first-order analysis indicates that bands n′ and p increase slightly in energy with increasing spessartine and decreasing almandine content in the solid solution. The opposite behavior is the case for bands n and o. However, we note that this result is a bit tentative, because of scatter in the data and/or incomplete data coverage for more spessartine-poor compositions.

**Spin-forbidden $Fe^{3+}$ transitions.** The energies of the three bands l, m, and r for several almandine-rich garnets are shown in Figure 5. $Fe^{3+}$-O bonding, based on the energies of these bands, is discussed below.

### Crystal chemistry and $Fe^{2+}$-O and $Mn^{2+}$-O bond behavior of almandine-pyrope and almandine-spessartine solid solutions

There are many research reports on aluminosilicate garnet, $\{X_3^{2+}\}[Al_2](Si_3)O_{12}$, at the microscopic scale. For solid solutions, atomic exchange occurs at $\{X^{2+}\}$ and it causes variations in local structure properties within the crystal. $X^{2+}$-O chemical bonding should be affected. Structural relaxation occurs within the triangular dodecahedron sublattice, but neighboring octahedra (and tetrahedra) are affected as well because they share polyhedral edges with the former (Fig. 1). A crystal-chemical analysis of solid-solution behavior is simplified in garnet, compared to many other silicates, because it has a high symmetry ($Ia\bar{3}d$) and by the fact that all three cations are located on special crystallographic positions and the single crystallographic anion ligand (i.e., oxygen) is located at a general $x$, $y$, $z$ position (Novak and Gibbs 1971; Armbruster et al. 1992; Merli et al. 1995). Thus, local structural relaxation is associated with the oxygen ions, as is macroscopic relaxation for the crystal as a whole.

Experimental studies have been made on how the two crystallographically independent $X^{2+}$-O bond lengths behave in binary solid solutions using X-ray absorption (Fe and Mn) fine structure spectroscopy (Sani et al. 2004) and NIR absorption spectroscopy of spin-allowed $Fe^{2+}$ bands (Geiger and Rossman 1994), as well by single-crystal diffraction methods (Armbruster et al. 1992). Bond behavior and local structural variations in garnet solid solutions have also been investigated computationally (e.g., Bosenick et al. 2000; Geiger et al. 2003; Freeman et al. 2006).

Sani et al. (2004) measured the $Fe^{2+}$-O and $Mn^{2+}$-O bond

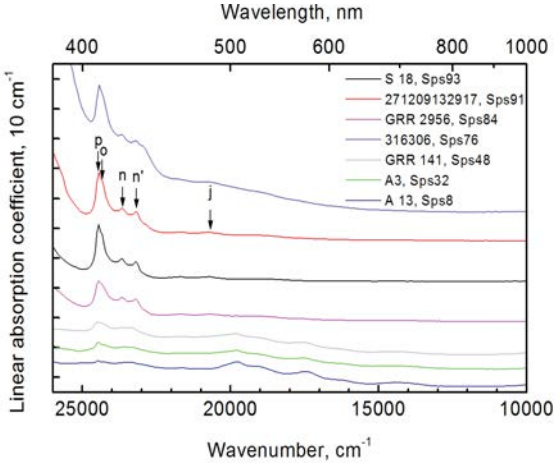


**Figure 4.** Stacked plot of spectra of various almandine-spessartine garnets. Aside from the spectrum of A-13, the spectra are shifted vertically for the sake of clarity. Note that the absorption behavior for the spessartine-rich garnets is not a simple function of the spessartine content. The arrows indicate several spin-forbidden bands related to $Mn^{2+}$ and the letters follow Moore and White (1972), as modified by Taran et al. (2023) (i.e., band n′). The $Mn^{2+}$ band intensities are not a well defined function of spessartine content in the garnet [see discussion of this aspect in Taran et al. (2023). (Color online.)

lengths for several synthetic almandine-spessartine garnets. The spectra indicated that the two different $Fe^{2+}$-O bonds did not vary in length, that is Fe(1)-O [or alternatively the label Fe-O(2)] were ~2.21 Å and Fe(2)-O [or Fe-O(4)] bonds were ~2.35 Å across the binary. In contrast, the shorter Mn(1)-O [or Mn-O(2)] bond remained constant in length with a value of ~2.24 Å, whereas the longer Mn(2)-O bond [or Mn-O(4)] increased slightly in length from about 2.37 Å to about 2.43 Å going from almandine-rich to more spessartine-rich garnet compositions. Geiger and Rossman (1994) investigated $Fe^{2+}$-O bond behavior for the almandine-pyrope and almandine-spessartine binaries by measuring the three highest energy spin-allowed absorption bands of $Fe^{2+}$ occurring in the NIR region. They originate from the split ${}^5E_g \rightarrow {}^5T_{2g}$ electronic transition for symmetry descending from $O_h$ (cubic) to $D_2$ (dodecahedral) [e.g., White and Moore (1972)—it should be noted that this latter type of spectroscopy is more sensitive to variations in bond length than the former, but numerical values cannot be obtained]. It was argued that $Fe^{2+}$-O bond length (note that the two crystallographically independent $Fe^{2+}$-O bonds could not be measured spectroscopically and that the analysis only considers a single undifferentiated $Fe^{2+}$-O bond) decreases slightly in length with increasing pyrope component in the garnet. This is expected because pyrope has a smaller molar volume [i.e., 11.3157(16) J/bar, where the radius of $Mg^{2+}$ = 0.89 Å—Geiger and Feenstra (1997) and Shannon (1976)] than almandine [i.e., 11.523(6) J/bar, where the radius of $Fe^{2+}$ = 0.92 Å]. In other words, a model of Pauling limit behavior (or the state of alternation bonds) involving slight $Fe^{2+}$-O bond shortening describes the behavior across the join (see Geiger 2008). The behavior of $Fe^{2+}$-O bonds in almandine-spessartine solid solutions was more difficult to interpret. Here, assuming Pauling limit behavior is operating, it could be expected that $Fe^{2+}$-O bonds should increase slightly in length with increasing spessartine in the garnet. This is because the molar volume of spessartine [i.e., 11.796(3) J/bar, where the radius of $Mn^{2+}$ = 0.96 Å (Geiger and Feenstra 1997; Shannon 1976)] is greater than that of almandine. However, the general increase in energy of at least two of the three $Fe^{2+}$ $T_{2g}$ bands with increasing spessartine in the garnet does not appear to support the assumed model behavior.

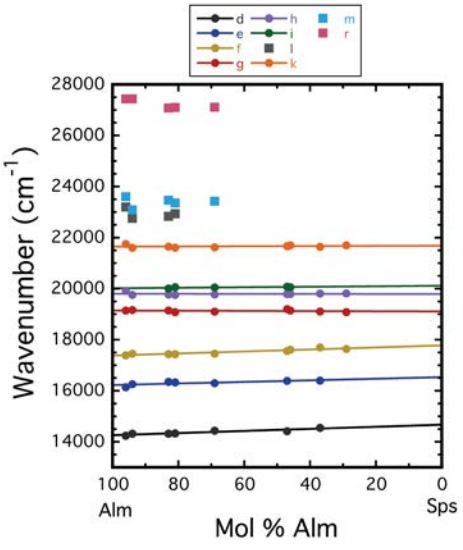


**Figure 5.** Wavenumbers for spin-forbidden bands related to $Fe^{2+}$ (solid circles) and $Fe^{3+}$ (solid squares) as a function of almandine mole percent (Online Materials[1] Table OM1b) for almandine-spessartine solid solutions. The size of the symbols is larger than the experimental uncertainty. The lines represent linear least-squares best fits to the energies for several lower energy bands. No fits were made to the energies of the three highest energy bands because of the limited data coverage. (Color online.)

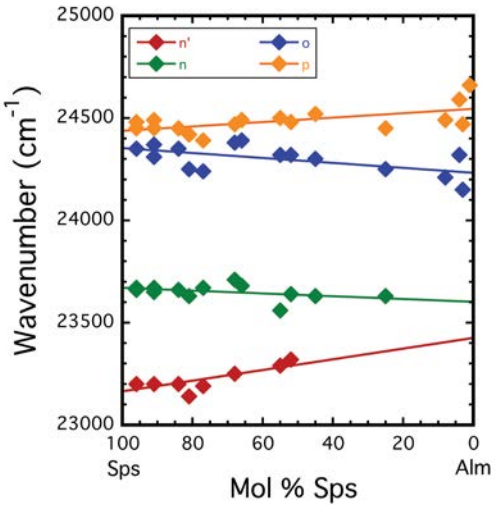


**Figure 6.** Wavenumbers for the most intense spin-forbidden bands related to $Mn^{2+}$ lying between 23 000 and 25 000 $cm^{-1}$ (n′, n, o, and p) as a function spessartine mole percent in the garnet (Online Materials[1] Table OM1b) for almandine-spessartine solid solutions. The size of the symbols is larger than the experimental uncertainty. The lines represent linear least-squares best fits to the energies of the different bands. (Color online.)

Consider now the present UV/Vis spectroscopic results and the energy behavior of the different $Fe^{2+}$ spin-forbidden transitions in almandine-pyrope garnets. An analysis of the transition energies indicates that variations as a function of garnet composition occur. Those of the lower wavenumber bands d, e, and f appear to decrease slightly between roughly 90 to 125 $cm^{-1}$ starting from nearly end-member almandine to nearly end-member pyrope (Fig. 3). The energy of the transition given by band g does not vary as a function of garnet composition. In contrast, bands h, i, and k appear to increase in energy (between 80 and 150 $cm^{-1}$) with increasing pyrope component in the garnet. Finally, the highest wavenumber transition, given by band q, increases the most by about 325 $cm^{-1}$ across the join.

These bands represent different spin-forbidden electronic transitions among the five split $Fe^{2+}$ $d$ orbitals occurring in the triangular dodecahedral crystal field. White and Moore (1972) analyzed geometrically the $d$ orbital placement within a cube (i.e., the triangular dodecahedron in garnet can be described as a distorted cube) with respect to the relative energies of the different spin-allowed $Fe^{2+}$ transitions. Geiger and Rossman (1994) and Geiger et al. (2003) modified their analysis taking into account a more recent and currently accepted transition scheme of Newman et al. (1978). Following this, the $d_z^2$ and $d_{xy}$ orbitals should have the least electronic repulsion with $O^{2-}$ ligands located at the cube corners, because the lobes of both orbitals point to the centers of cube faces.

The $d_z^2$ orbital is taken as the ground state and $d_{xy}$ the next highest energy for the two lowest energy $E_g$ split states of $Fe^{2+}$. For the three higher energy $T_{2g}$ split levels, the $d_{yz}$ orbital energy should be the most stable and $d_{xz}$ the least due to the $D_2$ geometry of the triangular dodecahedron. The orbital $d_{x2-y2}$ should be intermediate in energy between these two states. Following this and assuming, once again, a model of Pauling limit behavior involving slight local $Fe^{2+}$-O bond compression with increasing pyrope in a garnet crystal, it can be argued that those spin-forbidden $Fe^{2+}$ bands showing the greatest changes in energy with varying garnet composition should involve transitions between the $d_{yz}$, $d_{x2-y2}$, and $d_{xz}$ orbitals. In other words, these orbitals should be the most sensitive to local positional relaxation of the single $O^{2-}$ ligand in $x$, $y$ and $z$. The $Fe^{2+}$ electronic transition given by highest wavenumber band q could involve $d_{xz}$, because it should have the largest repulsion with the $p$ orbitals of $O^{2-}$. Those transitions that decrease slightly in energy with increasing pyrope component in the garnet (i.e., the lowest wavenumber bands d, e, and f) would involve local oxygen shifts in $x$, $y$ and $z$ that decrease the degree of iron orbital-oxygen orbital repulsion. The spectroscopic and diffraction results give a fairly consistent crystal-chemical picture of solid-solution behavior for almandine-pyrope garnets.

It is more difficult to construct a consistent crystal-chemical and bonding model for almandine-spessartine garnets, as based on the existing data. Here, the energy behavior of $Fe^{2+}$ spin-allowed bands (Geiger and Rossman 1994) does not support a crystal-chemical model with Pauling limit behavior, whereby local $Fe^{2+}$-O bonds increase in length with increasing spessartine in the garnet. What is the $Fe^{2+}$ spin-forbidden transition energy behavior for this solid solution and can it be explained? For this garnet system, the lowest wavenumber bands d, e, and f appear to vary the most in energy (i.e., between roughly 300 and 400 $cm^{-1}$) compared to those of the higher wavenumber transitions given by bands g, h, i, and k (i.e., <100 $cm^{-1}$). All transitions increase in energy with increasing spessartine in the garnet (Fig. 5). This is different than the general energy behavior exhibited by $Fe^{2+}$ electronic transitions in almandine-pyrope garnets, where energies can decrease or increase across the join.

The energy behavior of four higher wavenumber spin-forbidden $Mn^{2+}$ transitions (bands n′, n, o, and p) across the almandine-spessartine binary is shown in Figure 6. $Mn^{2+}$ has different electronic behavior compared to $Fe^{2+}$ because of the former's $d^5$ electronic configuration. Chemical bonding should also be different. Should the energy trends laid out by the data be correct, the behaviors of the four different $Mn^{2+}$ electronic transitions of relatively similar wavenumbers are dissimilar. It is difficult to interpret the spectroscopic results more fully because assignments for all the $Mn^{2+}$ electronic transitions have not been successful. A satisfactory analysis of spessartine's UV/Vis spectrum, based on crystal field theory and the use of Tanabe-Sugano diagrams with $O_h$ symmetry, cannot be obtained (Taran et al. 2023).

We conclude that the NIR and Vis/UV spectroscopic results on spin-allowed and spin-forbidden $Fe^{2+}$ electronic transitions, respectively, indicate that the transition energy behavior of this cation and its bonding with oxygen are different in almandine-pyrope and almandine-spessartine garnets. Obtaining a better understanding of electronic transition energy behavior is complex for a couple of reasons and further research is needed. The vibrational behavior of $Fe^{2+}$ in almandine is anisotropic in nature, as shown by X-ray diffraction and $^{57}Fe$ Mössbauer spectroscopic measurements on synthetic end-member almandine (Armbruster et al. 1992; Geiger et al. 1992) and a natural almandine solid-solution crystal (Bull et al. 2012). The interatomic potential involving $Fe^{2+}$ is probably fairly anharmonic as well (see Geiger 2013). It is not known how vibrational anisotropy and anharmonicity vary in almandine-bearing solid solutions and how they can affect local electronic-transition and chemical-bonding properties. Computational studies on pyrope-grossular, $\{Mg_{3x},Ca_{3-3x}\}[Al_2](Si_3)O_{12}$, solid solutions (Bosenick et al. 2000; Freeman et al. 2006) show that the longer X-O(4) bonds for both Mg and Ca vary more in length compared to shorter X-O(2) bonds across this garnet binary. Such calculations are needed on almandine-bearing garnet solid solutions.

It may be noted, in concluding and in a related sense, that $^{57}Fe$ Mössbauer measurements on almandine-containing binary solid solutions do not show significant variations in their hyperfine parameters (Geiger et al. 2003). Specifically, the isomer shift, which is a measure of the $s$ electron contact density at the $Fe^{2+}$ nucleus, and which is affected by the nature of and screening by the $d$ bonding orbitals, is not measurably different between $\{Mg_{3x}Fe^{2+}_{3-3x}\}$-$[Al_2](Si_3)O_{12}$ and $\{Mn^{2+}_{3x}Fe^{2+}_{3-3x}\}[Al_2](Si_3)O_{12}$ garnets [i.e., 1.27 ± 0.01 mm/s at RT and 1.41 ± 0.01 at 77 K (Geiger et al. 2003)]. The explanation for this observation is that the $Fe^{2+}$-O bonds are highly ionic (Lyubutin and Dodokin 1971; Evans and Sergent 1975; Geiger et al. op. cit.) and any covalent contributions, regardless of the garnet composition, are not reflected in the hyperfine parameters.

### $Fe^{3+}$ and $Fe^{3+}$-O bonding in aluminosilicate garnet

The study of Moore and White (1972) shows that $Fe^{3+}$ can be present in almandine, as based on their interpretation of the spin-forbidden $Fe^{3+}$ bands l, m, and r. Later works, both experimental (Smith and Langer 1983) and theoretical (Guo-Yin and Min-Guang 1984), challenged the assignments for these three bands especially for the most intense band r. We accept Moore and White's interpretation [see Taran et al. (2023) for a detailed discussion of these bands and their intensity behavior]. Following this and based on the spectra of this work, it appears that many, if not nearly all, almandine-pyrope garnets contain some $Fe^{3+}$. This is a notable result.

In terms of crystal chemistry, an analysis of $Fe^{3+}$-$O^{2-}$ bonding behavior is possible using the measured UV/Vis spectra and published results. A measure of the covalent bonding between a central ion and its surrounding ligands can be described by the Racah $B$ parameter [see discussion in Burns (1993)]. The other Racah parameter is $C$. The relevant equations are:

$$^6A_{1g} \rightarrow {}^4A_{1g}, {}^4E_g\ (^4G)\text{: } \nu_3 = 10B + 5C \quad (2)$$

and

$$^6A_{1g} \rightarrow {}^4E_g\ (^4D)\text{: } \nu_5 = 17B + 5C \quad (3)$$

from which one obtains:

$$\nu_5 - \nu_3 = 7B. \quad (4)$$

The energies of bands l and m and the energy of band r come into play. Consider garnet GTF 90-28 with about 71 mol% almandine, for example (Table 1a). Taking $\nu_3$ as the mean value

of the energies of the l and m bands, one obtains $B \approx 557$ and $C \approx 3522$ cm$^{-1}$. For the case of $^{VI}Fe^{3+}$ in grossular, one has 714 and 2972 cm$^{-1}$ using the spectral data in Moore and White (1972) (note that their published values of 614 and 3332 cm$^{-1}$ appear to be incorrect), and for $^{VI}Fe^{3+}$ in andradite 613 and 3308 cm$^{-1}$ (Platonov and Taran 2018). Because the *B* parameter is lowest for almandine, its $Fe^{3+}$-$O^{2-}$ bond is slightly more covalent compared to $Fe^{3+}$-$O^{2-}$ bonds in the Ca-rich garnets grossular and andradite. The $Fe^{3+}$-$O^{2-}$ bond length in end-member andradite is 2.0201(5) Å (Armbruster and Geiger 1993) and the $Al^{3+}$-$O^{2-}$ bond length is 1.8904(4) Å in end-member almandine (Armbruster et al. 1992). Thus, it should be expected that a local $Fe^{3+}$-$O^{2-}$ bond in almandine could be very slightly shorter than in andradite. Band r in the spectrum of andradite occurs at lower energy (i.e., 26 800 cm$^{-1}$) than in almandine (i.e., ~27 050 cm$^{-1}$).

The $Fe^{3+}$ bands l and m and r vary in energy more as a function of bulk garnet composition than $Fe^{2+}$-related bands (Fig. 3). The shorter $Fe^{3+}$-O chemical bonds should be more covalent than the longer $Fe^{2+}$-O bonds and the electronic state of $Fe^{3+}$ is apparently more affected by its crystal-chemical surroundings than $Fe^{2+}$ (Figs. 1b and 1d). The longer $Fe^{2+}$-O bonds should be highly ionic in nature and the electronic state of $Fe^{2+}$ is affected little by changes in its immediate ligand surroundings.

## Implications

The microscopic properties and crystal-chemical behavior of various silicate garnet solid-solution systems are slowly being revealed with time. Further study of a more quantitative nature, compared to what has been done in the past, is now needed.

From an experimental standpoint, several areas of research could be done. First, work is required to better standardize spectra. There is no consensus on how to report UV/Vis band energies and their uncertainties. Large numbers of spectra on garnet have been recorded over many years using many different experimental setups, but it is difficult to compare and analyze reported band energies. Standards, as used in most types of experimental measurements, are required. Second, further spectroscopic measurements on other solid-solution aluminosilicate garnets are needed. This is necessary to obtain a broader and more systematic description of $Fe^{2+}$ and $Mn^{2+}$ electronic and chemical-bonding behavior. Variations in local properties and structural heterogeneity in almandine-pyrope-spessartine garnets can be expected to be considerably greater with the incorporation of the large $Ca^{2+}$ cation when it replaces $Fe^{2+}$, Mg, and $Mn^{2+}$. It remains to be determined how $Fe^{2+}$ and $Mn^{2+}$ electronic transitions, spin allowed for $Fe^{2+}$ and spin forbidden for both cations, will be affected. Third, the nature of band broadening for spin-forbidden and spin-allowed transitions in intermediate composition garnets has not been explored. Both could possibly carry some information on local structural heterogeneity through their band widths. As best we know, there has been little, if any, research made in this direction at least in terms of minerals. Fourth, more study relating to $Fe^{3+}$ contents in aluminosilicate garnets, using UV/Vis spectra obtained with a microscope, could prove interesting. Determining small $Fe^{3+}$ contents from microprobe analyses and assuming stochiometric considerations are fraught with uncertainty. $^{57}$Fe Mössbauer measurements are typically made using powders and, thus, zoning determinations in crystals cannot be undertaken. Moreover, the method is not precise at small $Fe^{3+}$ concentrations. X-ray absorption studies (XANES) on $Fe^{3+}$ amounts require access to a synchrotron and the interpretation and fitting of spectra are not necessarily straightforward.

Finally, there exists little work on interpreting the spectra of complex silicates using advanced bonding theories and state-of-the-art electronic structure calculations. Studies combining quantitative spectroscopic measurements with simulations will yield a deeper physical understanding of electronic transition and bonding behavior. In terms of garnet solid solutions, local structural relaxation behavior and how it affects bonding needs study. Many experimental results alone are either too blunt or are difficult to quantify for such subtle structural variations. To begin, electronic structure calculations on end-member spessartine and almandine should be possible. Studying garnet solid-solution systems will be a greater challenge.

## Acknowledgments

Several different individuals and sources provided garnet samples used in this study. In the cases where they are known, they are listed in Tables 1a and 1b. We thank the various institutions and individuals for their generosity. We also thank O.A. Vyshnevskyi (Kyiv) for making microprobe EDS analyses on the samples studied spectroscopically in Kyiv and M. Grodzicki (Salzburg) for helpful discussions on crystal/ligand field theory. U. Hålenius and an anonymous referee are thanked for their useful comments that improved the manuscript.

## Funding

This research was supported by a grant to C.A.G. from the Austrian Science Fund (FWF: P 30977-NBL). He also thanks the "Land Salzburg" for financial support through the initiative "Wissenschafts- und Innovationsstrategie Salzburg 2025."

## References cited

Aparicio, C., Filip, J., Skogby, H., Marusak, Z., Mashlan, M., and Zboril, R. (2012) Thermal behavior of almandine at temperatures of 1,200 °C in hydrogen. Physics and Chemistry of Minerals, 39, 311–318, https://doi.org/10.1007/s00269-012-0488-x.

Armbruster, T. and Geiger, C.A. (1993) Andradite crystal chemistry, dynamic X-site disorder and structural strain in silicate garnets. European Journal of Mineralogy, 5, 59–72, https://doi.org/10.1127/ejm/5/1/0059.

Armbruster, T., Geiger, C.A., and Lager, G.A. (1992) Single crystal X-ray refinement of almandine pyrope garnets at 298 and 100 K. American Mineralogist, 77, 512–523.

Boeke, H.E. (1914) Die Granatgruppe. Eine statistische Untersuchung. Zeitschrift für Kristallographie, 53, 149–157.

Boiocchi, M., Bellatreccia, F., Della Ventura, G., and Oberti, R. (2012) On the symmetry and atomic ordering in (OH,F)-rich spessartine: Towards a new hydrogarnet end-member. Zeitschrift für Kristallographie. Crystalline Materials, 227, 385–395, https://doi.org/10.1524/zkri.2012.1487.

Bosenick, A., Dove, M.T., and Geiger, C.A. (2000) Simulation studies of pyrope-grossular solid solutions. Physics and Chemistry of Minerals, 27, 398–418, https://doi.org/10.1007/s002690000088.

Bressler, C.T. (1945/1946) Garnet deposits near Wrangell southeastern Alaska. Geological Survey Bulletin, 963-C, 81–93.

Bull, J.N., Tennant, W.C., Ballaran, T.B., Nestola, F., and McCammon, C.A. (2012) Anisotropic mean-squared-displacement tensor in cubic almandine garnet: A single crystal $^{57}$Fe Mössbauer study. Physics and Chemistry of Minerals, 39, 561–575, https://doi.org/10.1007/s00269-012-0512-1.

Burns, R.G. (1970) Mineralogical Applications of Crystal Field Theory, 224 p. Cambridge University Press.

——— (1993) Mineralogical Applications of Crystal Field Theory, 2nd ed., 576 p. Cambridge University Press.

Clark, S.P. Jr. (1957) Absorption spectra of some silicates in the visible and near infrared. American Mineralogist, 42, 732–742.

Čopjaková, R., Sulovský, P., and Paterson, B. (2005) Major and trace elements in pyrope-almandine garnets as sediment provenance indicators of the Lower Carboniferous Culm sediments, Drahany Uplands, Bohemia Massif. Lithos, 82, 51–70, https://doi.org/10.1016/j.lithos.2004.12.006.

Dachs, E., Geiger, C.A., and Benisek, A. (2012) Almandine: Lattice and non-lattice heat capacity behavior and standard thermodynamic properties. American Mineralogist, 97, 1771–1782, https://doi.org/10.2138/am.2012.4163.

Deer, W.A., Howie, R.A., and Zussman, J. (1982) Orthosilicates (Rock Forming Minerals) (v. 1A) 2nd ed., 932 p. Geological Society of London.

Evans, B.J. and Sergent, E.W. Jr. (1975) $^{57}$Fe NGR of Fe phases in "magnetic cassiterites." Contributions to Mineralogy and Petrology, 53, 183–194, https://doi.org/10.1007/BF00372603.

Freeman, C.L., Allan, N.L., and van Westrenen, W. (2006) Local cation environments in the pyrope-grossular $Mg_3Al_2Si_3O_{12}$-$Ca_3Al_2Si_3O_{12}$ garnet solid solution. Physical Review B: Condensed Matter and Materials Physics, 74, 134203–1, https://doi.org/10.1103/PhysRevB.74.134203.

Geiger, C.A. (2004) Spectroscopic investigations relating to the structural, crystal-chemical and lattice-dynamic properties of $(Fe^{2+},Mn^{2+},Mg,Ca)_3Al_2Si_3O_{12}$ garnet: A review and analysis. In E. Libowitzky and A. Beran, Eds., European Notes in Mineralogy, 6, 589–645. Mineralogical Society of Great Britain and Ireland.

——— (2008) Silicate garnet: A micro to macroscopic (re)view. American Mineralogist, 93, 360–372, https://doi.org/10.2138/am.2008.2588.

——— (2013) Static disorders of atoms and experimental determination of Debye temperature in pyrope: Low- and high-temperature single-crystal X-ray diffraction study—Discussion. American Mineralogist, 98, 780–782, https://doi.org/10.2138/am.2013.4301.

——— (2016) A tale of two garnets: The role of solid solution in the development toward a modern mineralogy. American Mineralogist, 101, 1735–1749, https://doi.org/10.2138/am-2016-5522.

Geiger, C.A. and Feenstra, A. (1997) Molar volumes of mixing of almandine-pyrope and almandine-spessartine garnets and the crystal chemistry and thermodynamic-mixing properties of the aluminosilicate garnets. American Mineralogist, 82, 571–581, https://doi.org/10.2138/am-1997-5-617.

Geiger, C.A. and Rossman, G.R. (1994) Crystal field stabilization energies of almandine-pyrope and almandine-spessartine garnets determined by FTIR near infrared measurements. Physics and Chemistry of Minerals, 21, 516–525, https://doi.org/10.1007/BF00203926.

——— (2018) IR spectroscopy and $OH^-$ in silicate garnet: The long quest to document the hydrogarnet substitution. American Mineralogist, 103, 384–393, https://doi.org/10.2138/am-2018-6160CCBY.

Geiger, C.A. and Taran, M.N. (2023) Single-crystal UV/Vis absorption spectroscopy of aluminosilicate garnet: Part III. $\{Fe^{2+}\} + [Fe^{3+}] \rightarrow \{Fe^{3+}\} + [Fe^{2+}]$ intervalence charge transfer. American Mineralogist, 108, 1171–1181.

Geiger, C.A., Armbruster, T., Lager, G.A., Jiang, K., Lottermoser, W., and Amthauer, G. (1992) A combined temperature dependent $^{57}$Fe Mössbauer and single crystal X-ray diffraction study of synthetic almandine: evidence for the Gol'danskii-Karyagin effect. Physics and Chemistry of Minerals, 19, 121–126, https://doi.org/10.1007/BF00198609.

Geiger, C.A., Stahl, A., and Rossman, G.R. (2000) Single-crystal IR- and UV/VIS-spectroscopic measurements on transition-metal-bearing pyrope: The incorporation of hydroxide in garnet. European Journal of Mineralogy, 12, 259–271, https://doi.org/10.1127/0935-1221/2000/0012-0259.

Geiger, C.A., Grodzicki, M., and Amthauer, G. (2003) The crystal chemistry and $Fe^{II}$ site properties of aluminosilicate garnet solid solutions as revealed by Mössbauer spectroscopy and electronic structure calculations. Physics and Chemistry of Minerals, 30, 280–292, https://doi.org/10.1007/s00269-003-0319-1.

Guo-Yin, S. and Min-Guang, Z. (1984) Analysis of the spectrum of $Fe^{2+}$ in Fe-pyrope garnets. Physical Review B: Condensed Matter, 30, 3691–3703, https://doi.org/10.1103/PhysRevB.30.3691.

Hickmott, D.D., Shimizu, N., Spear, F.S., and Selverstone, J. (1987) Trace-element zoning in a metamorphic garnet. Geology, 15, 573–576, https://doi.org/10.1130/0091-7613(1987)15<573:TZIAMG>2.0.CO;2.

Khomenko, V.M., Langer, K., Wirth, R., and Weyer, B. (2002) Mie scattering and charge transfer phenomena as causes of the UV edge in the absorption spectra of natural and synthetic almandine garnets. Physics and Chemistry of Minerals, 29, 201–209, https://doi.org/10.1007/s00269-001-0225-3.

Korinevsky, V.G. (2015) Spessartine-andradite in scapolite pegmatite, Ilmeny Mountains, Russia. Canadian Mineralogist, 53, 623–632, https://doi.org/10.3749/canmin.4354.

Krambrock, K., Guimarães, F.S., Pinheiro, M.V.B., Paniago, R., Righi, A., Persiano, A.I.C., Karfunkel, J., and Hoover, D.B. (2013) Purplish-red almandine garnets with alexandrite-like effect: Causes of colors and color-enhancing treatments. Physics and Chemistry of Minerals, 40, 555–562, https://doi.org/10.1007/s00269-013-0592-6.

Lyubutin, I.S. and Dodokin, A.P. (1971) Temperature dependence of the Mössbauer effect for $Fe^{2+}$ in dodecahedral coordination in garnet. Soviet Physics, Crystallography, 15, 1091–1092.

Manning, P.G. (1967) The optical absorption spectra of the garnets almandine-pyrope, pyrope, and spessartine and some structural interpretations of mineralogical significance. Canadian Mineralogist, 9, 237–251.

——— (1972) Optical absorption spectra of $Fe^{3+}$ in octahedral and tetrahedral sites in natural garnets. Canadian Mineralogist, 11, 826–839.

Manson, D.V. and Stockton, C.M. (1984) Pyrope-spessartine garnets with unusual color behavior. Gems & Gemology, 20, 200–207, https://doi.org/10.5741/GEMS.20.4.200.

Marfunin, A.S. (1979) Physics of Mineral and Inorganic Materials, 342 p. Springer.

Merli, M., Callegari, A., Cannillo, E., Caucia, F., Leona, M., Oberti, R., and Ungaretti, L. (1995) Crystal-chemical complexity in natural garnets: Structural constraints on chemical variability. European Journal of Mineralogy, 7, 1239–1250, https://doi.org/10.1127/ejm/7/6/1239.

Moore, R.K. and White, W.B. (1972) Electronic spectra of transition metal ions in silicate garnets. Canadian Mineralogist, 11, 791–811.

Newman, D.J., Price, D.D., and Runciman, W.A. (1978) Superposition model analysis of the near infrared spectrum of $Fe^{2+}$ in pyrope-almandine garnets. American Mineralogist, 63, 1278–1281.

Novak, G.A. and Gibbs, G.V. (1971) The crystal chemistry of the silicate garnets. American Mineralogist, 56, 791–825.

Pabst, A. (1943) Large and small garnets from Fort Wrangell, Alaska. American Mineralogist, 28, 233–245.

Pinet, M. and Smith, D.C. (1994) Raman microspectrometry of garnets $X_3Y_2Z_3O_{12}$: II. The natural aluminium series pyrope-almandine-spessartine. Schweizerische Mineralogische und Petrographische Mitteilungen, 74, 161–179.

Platonov, A.N. and Taran, M.N. (2018) Optical Spectra and Color of Natural Garnets, 254 p. Naukova dumka, Kyiv (in Russian).

Runciman, W.A. and Marshall, M. (1975) The magnetic circular dichroism of pyrope-almandine garnets. American Mineralogist, 60, 1122–1124.

Runciman, W.A. and Sengupta, D. (1974) The spectrum of $Fe^{2+}$ ions in silicate garnets. American Mineralogist, 59, 563–566.

Sani, A., Quartieri, S., Boscherini, F., Antonioli, G., Feenstra, A., and Geiger, C.A. (2004) $Fe^{2+}$-O and $Mn^{2+}$-O bonding and $Fe^{2+}$- and $Mn^{2+}$-vibrational properties in synthetic almandine-spessartine solid solutions: An X-ray absorption fine structure study. European Journal of Mineralogy, 16, 801–808, https://doi.org/10.1127/0935-1221/2004/0016-0801.

Schmetzer, K., Hainschwang, T., Kiefert, L., and Bernhardt, H.-J. (2001) Pink to pinkish orange malaya garnets from Bekily, Madagascar. Gems & Gemology, 37, 296–308, https://doi.org/10.5741/GEMS.37.4.296.

Schwandt, C.S., Papike, J.J., and Shearer, C.K. (1996) Trace element zoning in pelitic garnet of the Black Hills, South Dakota. American Mineralogist, 81, 1195–1207, https://doi.org/10.2138/am-1996-9-1018.

Shannon, R.D. (1976) Revised effective ionic radii and systematic studies of interatomic distances in halides and chalcogenides. Acta Crystallographica, A32, 751–767, https://doi.org/10.1107/S0567739476001551.

Slack, G.A. and Chrenko, R.M. (1971) Optical absorption of natural garnets from 1000 to 30000 wavenumbers. Journal of the Optical Society of America, 61, 1325–1329, https://doi.org/10.1364/JOSA.61.001325.

Smith, G. and Langer, K. (1983) High pressure spectra up to 120 kbars of the synthetic garnet end members spessartine and almandine. Neues Jahrbuch für Mineralogie Monatshefte, 12, 541–555.

Sobolev, N.V. (1964) Classification of rock-forming garnets. Doklady Akademii Nauk SSSR, 157, 353–356.

Swanson, S.E. and Veal, W.B. (2010) Mineralogy and petrogenesis of pegmatites in the Spruce Pine District, North Carolina, U.S.A. Journal of Geosciences (Prague), 55, 27–42.

Taran, M.N., Langer, K., and Geiger, C.A. (2002) Single-crystal electronic absorption spectroscopy of synthetic chromium-, cobalt-, and vanadium-bearing pyropes at different temperatures and pressures. Physics and Chemistry of Minerals, 29, 362–368, https://doi.org/10.1007/s00269-002-0239-5.

Taran, M.N., Dyar, M.D., and Matsyuk, S.S. (2007) Optical absorption study of natural garnets of almandine-skiagite composition showing intervalence $Fe^{2+} + Fe^{3+} \rightarrow Fe^{3+} + Fe^{2+}$ charge-transfer transition. American Mineralogist, 92, 753–760, https://doi.org/10.2138/am.2007.2163.

Taran, M.N., Geiger, C.A., Vyshnevskyi, O.A., and Rossman, G.R. (2023) Single-crystal UV/Vis optical absorption spectra of almandine-bearing and spessartine garnet: Part II. An analysis of the spin-forbidden bands of $Fe^{2+}$, $Mn^{2+}$, and $Fe^{3+}$. American Mineralogist, 108, 1161–1170.

White, W.B. and Moore, R.K. (1972) Interpretation of the spin-allowed bands of $Fe^{2+}$ in silicate garnets. American Mineralogist, 57, 1692–1710.

Woodland, A.B., Droop, G., and O'Neill, H.St.C. (1995) Almandine-rich garnet from near Collobrières, southern France, and its petrological significance. European Journal of Mineralogy, 7, 187–194, https://doi.org/10.1127/ejm/7/1/0187.

Zhou, K.-W. and Zhao, S.-B. (1984) The spin-forbidden spectrum of $Fe^{2+}$ in silicate garnets. Journal of Physics C: Solid State Physics, 17, 4625–4632, https://doi.org/10.1088/0022-3719/17/26/012.

Manuscript received February 22, 2022
Manuscript accepted July 27, 2022
Accepted manuscript online August 3, 2022
Manuscript handled by Simon Redfern

## Endnote:

[1]Deposit item AM-23-68499, Online Materials. Deposit items are free to all readers and found on the MSA website, via the specific issue's Table of Contents (go to http://www.minsocam.org/MSA/AmMin/TOC/2023/Jun2023_data/Jun2023_data.html).